Check for updates

Angewandte Chemie International Edition

Angewandte International Edition Chemie

How to cite: *Angew. Chem. Int. Ed.* **2026**, e9809366
doi.org/10.1002/anie.9809366

RESEARCH ARTICLE

Raman Self-Tracking Copper Metal-Organic Framework-Based Nanoplatform for Cuproptosis Cancer Therapy

Yujie Duan[1,2] | Ying Bao[1] | Ziwen Gao[3] | Xidong He[4] | Xinming Liu[1] | Hao Wang[1] | Chunsheng Xiao[1,2] | Xuesi Chen[1,2]

[1]State Key Laboratory of Polymer Science and Technology, Key Laboratory of Polymer Ecomaterials, Changchun Institute of Applied Chemistry, Chinese Academy of Sciences, Changchun, P. R. China | [2]School of Applied Chemistry and Engineering, University of Science and Technology of China, Hefei, P. R. China | [3]Department of Breast Surgery, Second Hospital of Jilin University, Changchun, P. R. China | [4]Department of Diagnostic Radiology, Yong Loo Lin School of Medicine, National University of Singapore, Singapore, Singapore

Correspondence: Ying Bao (bying@ciac.ac.cn) | Hao Wang (wangh@ciac.ac.cn) | Chunsheng Xiao (xiaocs@ciac.ac.cn) | Xuesi Chen (xschen@ciac.ac.cn)

Received: 12 May 2026 | **Revised:** 25 August 2026 | **Accepted:** 26 September 2026

Keywords: anticancer nanomedicines | cancer therapy | cuproptosis | metal-organic frameworks | Raman imaging

ABSTRACT

Cuproptosis represents a promising strategy for cancer therapy, yet its clinical translation is hampered by unexpected deactivation and off-target toxicity of copper ions during their delivery to tumors. We developed a copper metal-organic framework-based nanoplatform (CuF) with H_2O_2 responsiveness and Raman self-tracking capability for cuproptosis-mediated antitumor therapy. CuF was prepared by coordinating Cu^{2+} with an alkyne-bearing ligand, followed by PEGylation and incorporation of an iron-based catalyst. CuF undergoes catalyst-mediated oxidative cleavage of alkynyl bonds under tumor-associated elevated H_2O_2 levels, causing CuF degradation and Cu^{2+} release. Released Cu^{2+} causes copper overload in tumor cells, thereby inducing potent cuproptosis. Meanwhile, the resultant aldehydes and acids generated by the oxidative cleavage of alkynes can further synergistically potentiate cuproptosis. Consequently, CuF demonstrated high antitumor efficacy in a 4T1 tumor-bearing mouse model (with a tumor inhibition rate of 91%). Moreover, alkynes in the metal-organic framework (MOF) backbone provided an intrinsically enhanced Raman signal, enabling label-free self-tracking of CuF distribution and degradation in cells and tissue sections through Raman imaging. Overall, this work not only provides a new paradigm for cuproptosis-based anticancer agents, but also offers a versatile strategy for engineering H_2O_2 responsive materials and Raman imaging nanoplatforms.

1 | Introduction

Cuproptosis, a copper-dependent form of cell death first reported in 2022, offers a promising approach for cancer therapy [1]. Mechanistically, it utilizes copper ionophores to transport extracellular Cu^{2+} into mitochondria, where Cu^{2+} binds to lipoylated proteins in the tricarboxylic acid (TCA) cycle. This binding induces oligomerization of the proteins, leading to the loss of iron-sulfur cluster proteins, proteotoxic stress, and ultimately, cell death. However, current cuproptosis-based therapies face challenges. Endogenous copper-dependent ionophores including elesclomol (ES) [2], disulfiram [3, 4], and pyridine derivatives [5, 6] are constrained by limited antitumor efficiency and potential neurotoxicity [7]. Copper-containing nanoparticles prepared via electrostatic adsorption or liposome encapsulation are susceptible to interference from endogenous amino acids, thiols, or metal ions, leading to premature drug inactivation or systemic toxicity [8–12]. Therefore, the targeted delivery of Cu^{2+} to tumors to

All rights reserved, including rights for text and data mining and training of artificial intelligence technologies or similar technologies.
© 2026 Wiley-VCH GmbH

address the limitations of unexpected deactivation and off-tumor toxicities is urgently needed.

Copper metal-organic frameworks (Cu-MOFs) are Cu^{2+}-rich porous materials, which are generally stable under physiological conditions and can effectively shield Cu^{2+} from deactivation by endogenous ligands, offering a promising platform for targeted delivery of Cu^{2+} to induce cuproptosis in vivo [13, 14]. Very recently, our group demonstrated that alkyne-containing covalent organic frameworks (COFs) can serve as sensitive Raman probes due to the enhanced Raman scattering cross-section derived from interlayer molecular stacking [15]. Thus, we speculate that incorporating alkynyl groups into Cu-MOFs could endow Cu-MOFs with Raman imaging-based self-tracking ability, which will reveal the biological fate of Cu-MOFs and provide critical data for their clinical translation. However, due to the highly crystalline structure, sensitive degradation of Cu-MOFs in vivo to release Cu^{2+} has always been a significant challenge [16–19]. Meanwhile, metal–ligand coordination and interligand π–π stacking facilitate electron delocalization within the MOF, elevate the electron density of the alkyne moiety, and render the alkyne group in the MOF particularly susceptible to oxidation [20–25]. Given the elevated H_2O_2 level in the tumor microenvironment [26–29], we propose to investigate whether H_2O_2 can cleave the alkynyl bonds in MOFs under physiological conditions, thereby enabling responsive Cu^{2+} release in tumors. To our knowledge, the oxidative cleavage of alkynyl bonds in vivo has not yet been realized [30].

Herein, we present an alkyne-containing Cu-MOF nanoplatform with Raman self-tracking and H_2O_2-responsive properties for cuproptosis antitumor therapy (Scheme 1). Firstly, PCN-61 nanoparticles were synthesized by reacting 5,5',5''-(benzene-1,3,5-triyltris(ethyne-2,1-diyl))triisophthalic acid (BTEI) with Cu^{2+}, using phosphoric acid (H_3PO_4) as the end-capping agent. The resulting nanoparticle was then PEGylated with phosphate-terminated methoxy poly(ethylene glycol) (mPEG-P) and loaded with a catalyst, $[Fe(MeCN)_6(BF_4)_2]$, to afford the corresponding Cu-MOF nanoplatform, denoted as CuF (Scheme 1a). The obtained CuF possessed a bioorthogonal Raman signal at 2228 cm^{-1} (assigned to alkynyl group), enabling ultrasensitive label-free Raman imaging of CuF in tumor cells and tumor tissues (Scheme 1b). Moreover, CuF exhibited high stability under normal physiological conditions, a property that could prevent its premature deactivation in the circulatory system. Interestingly, the incorporation of catalyst $[Fe(MeCN)_6(BF_4)_2]$ enables oxidation of the alkynyl groups in CuF at pathologically relevant H_2O_2 levels, representing the first example of the H_2O_2-triggered oxidation of alkyne bond in vivo. This catalytic oxidation could degrade the frameworks, leading to the selective release of Cu^{2+} and the generation of aldehyde and carboxylic acid products to synergistically trigger cuproptosis in tumor cells (Scheme 1c). Additionally, the oxidation process also altered the Raman signal ratio between the alkyne (2228 cm^{-1}) and the aromatic ring (1588 cm^{-1}), allowing Raman imaging of collected tumor sections to assess the intratumoral distribution and stimulus-responsive degradation of CuF. Finally, in a subcutaneous breast cancer model, CuF exhibited potent antitumor effects through cuproptosis, achieving a 91% tumor inhibition rate.

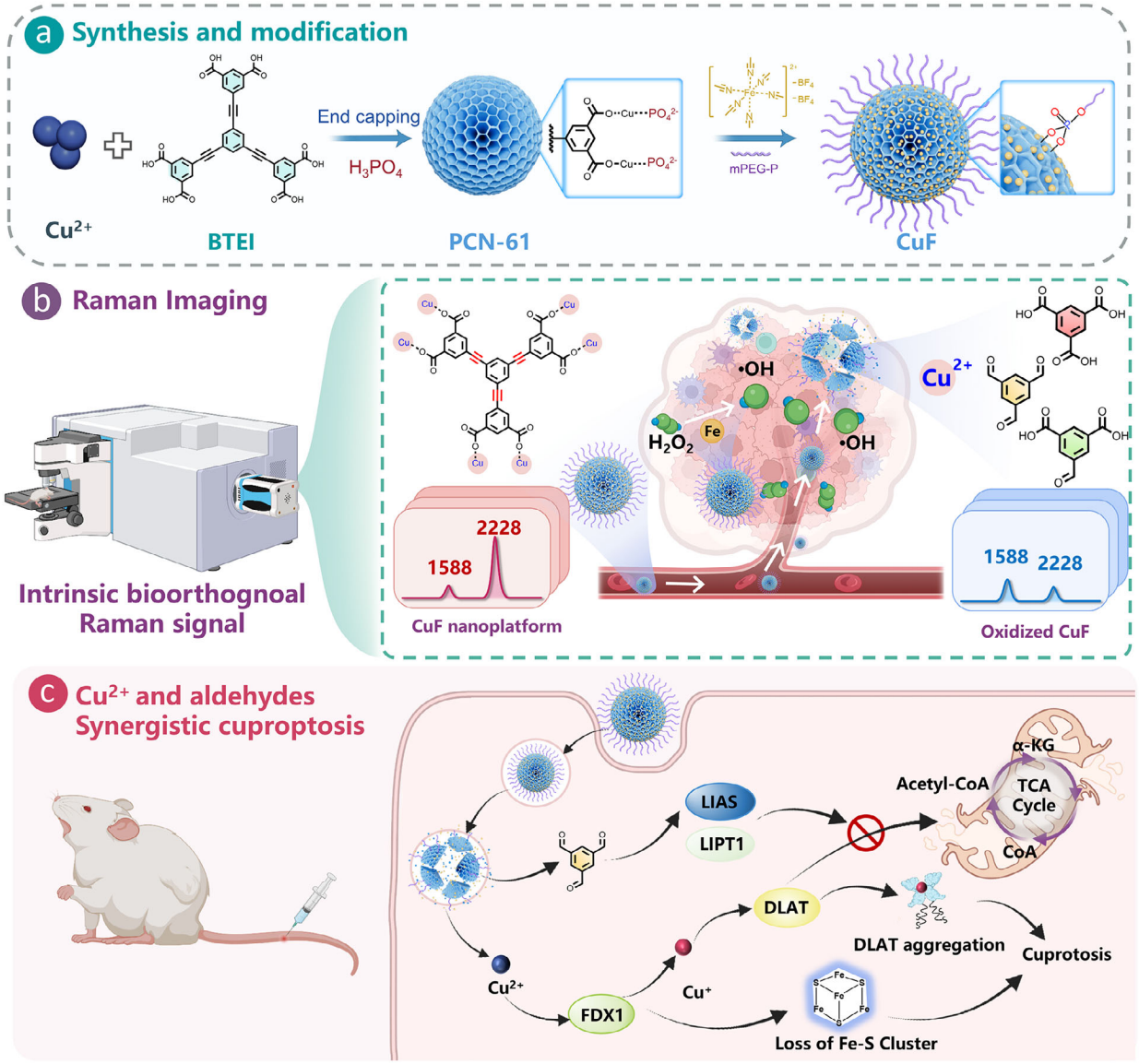
2 | Results and Discussion

2.1 | Synthesis and Characterization of Cu-MOF Nanoparticles

Alkyne-containing Cu-MOFs, designated as PCN-61, were selected as the starting materials and synthesized by coordination reaction between BTEI and Cu^{2+} (Figure 1a,b) [19]. However, direct synthesis of PCN-61 according to the reported method yielded micrometer-scale block-like or rod-like morphologies (Figures S1a and S1b), which are unsuitable for in vivo applications. Therefore, to modulate the particle size and morphology of PCN-61, we screened several capping agents during the synthesis (Table S1). As shown in Figure S1c–S1e, PCN-61 synthesized with benzoic acid, HBF_4, or acetic acid as capping agents suffered from aggregation and exhibited diameters exceeding 400 nm. Meanwhile, employing alendronic acid, phytic acid, hyaluronic acid, or alginate as capping agents failed to yield well-crystallized PCN-61 (Figure S2). Interestingly, when H_3PO_4 was used as the capping agent, spherical PCN-61 nanoparticles with a size of 81 nm were successfully obtained (Figure S1f). Next, to further improve the dispersibility and stability of PCN-61 nanoparticles in aqueous media, we performed surface ligand exchange using mPEG-P under ultrasonication (Figures S3–S5). The obtained nanoparticles, named CuP, exhibited a spherical morphology, with an average particle size of 86 nm and a surface potential of –15 mV (Figures 1c,d and S6). Moreover, CuP showed excellent dispersibility and remained stable in aqueous solution up to 48 h, whereas a large amount of precipitate was observed for PCN-61 nanoparticles without PEGylation (Figure S7). Powder x-ray diffraction (PXRD) confirmed that the surface modification with mPEG-P did not alter the crystal structure of the MOF core (Figure S2i). X-ray photoelectron spectroscopy (XPS) confirmed that the copper in CuP remained in the divalent state (Figure 1e–g).

Owing to the presence of alkyne in the framework, we hypothesized that the as-obtained CuP would exhibit a bioorthogonal Raman signal analogous to the COF-based Raman probes we recently reported [15]. As shown in Figure 1h, CuP displays a distinct Raman signal at 2228 cm^{-1} assigned to the alkynyl group. This peak falls within the bioorthogonal Raman-silent region (1800–2300 cm^{-1}), where no endogenous biomolecules exhibit Raman peaks, thus providing a high signal-to-noise ratio that is favorable in complex biological matrices [15, 31]. Moreover, the Raman signal intensity of CuP is significantly enhanced compared with that of the BTEI monomer. The RIE of CuP, calculated as the Raman intensity relative to the commonly used alkyne-containing Raman probe 5-ethynyl-2'-deoxyuridine (5-EdU), reached 1.24×10^4, which is comparable to other rationally designed polymer- or framework-based bioorthogonal Raman probes (Figure 1i) [15, 31]. Quantum-chemical calculations based on a PCN-61-derived finite-cluster model suggest that metal–ligand interactions may contribute to this enhancement by reorganizing the frontier-orbital distribution of the BTEI linkers and increasing the polarizability derivatives along the aromatic-ring and C≡C stretching normal coordinates (Figure S8a). Consistently, the normalized cumulative Raman activity of the C≡C vibrational modes in the PCN-61 cluster model

15213773, 0, Downloaded from https://onlinelibrary.wiley.com/doi/10.1002/anie.98093366 by National University Of Singapore, Wiley Online Library on [12/11/2026]. See the Terms and Conditions (https://onlinelibrary.wiley.com/terms-and-conditions) on Wiley Online Library for rules of use; OA articles are governed by the applicable Creative Commons License



SCHEME 1 | Schematic illustration of the preparation of CuF for Raman self-tracking cuproptosis-mediated tumor therapy. (a) CuF is prepared by reaction between BTEI and Cu^{2+}, loaded with the catalyst $[Fe(MeCN)_6(BF_4)_2]$, and surface-coated with mPEG-P. (b) Raman imaging for tracking the biodistribution and degradation of CuF, based on signal intensities at 2228 cm^{-1} and 1588 cm^{-1}. (c) In tumors, CuF undergoes catalyst-mediated responsive degradation in the presence of H_2O_2, releasing Cu^{2+} and other degradation products, which synergistically induces cuproptosis.

reached 124.214 a.u., approximately 10.2-fold higher than that calculated for the BTEI solution model (12.175 a.u.) (Figure S8b). This coordination-induced electronic contribution is conceptually consistent with charge-transfer-mediated enhancement of the Raman polarizability response reported previously [15, 32]. Moreover, the Raman signal peak intensity displays good linearity with CuP concentration ranging from 72 to 1440 μM (Figures 1j and S9), which provides a convenient basis for Raman-based quantitative concentration analysis of CuP within the validated quantification range.

2.2 | Catalyst-Mediated Oxidative Degradation of Cu-MOF Nanoparticles

To achieve tumor-selective cuproptosis, copper carriers should remain inert in normal tissues but undergo stimuli-responsive release of Cu^{2+} in tumors [33, 34]. Due to the rapid metabolism, tumors possess a relatively high concentration of H_2O_2 (typically 10–100 μM), which provides a potential trigger for responsive drug release [26, 28, 35–37]. Interestingly, as unsaturated bonds with high electron density, alkynes are potential moieties susceptible to oxidative cleavage by H_2O_2 [38, 39]. Notably, the alkyne bond in CuP is a diaryl alkyne embedded in a conjugated MOF backbone; both intralayer and interlayer conjugative delocalization in the MOF render the alkyne even more susceptible to oxidation, particularly radical-mediated single-electron transfer oxidation processes [24, 40]. Although the alkyne is already the most readily oxidatively cleavable bond in CuP, its oxidation scarcely proceeds under catalyst-free conditions. The inherent stability of CuP renders it resistant to degradation even at the highest tumor-related H_2O_2 concentrations (Figure S10). To fully utilize H_2O_2 in the tumor microenvironment [37] and achieve MOF degradation under physiological conditions, it is imperative to introduce a

15213773, 0, Downloaded from https://onlinelibrary.wiley.com/doi/10.1002/anie.9809366 by National University Of Singapore, Wiley Online Library on [12/11/2026]. See the Terms and Conditions (https://onlinelibrary.wiley.com/terms-and-conditions) on Wiley Online Library for rules of use; OA articles are governed by the applicable Creative Commons License

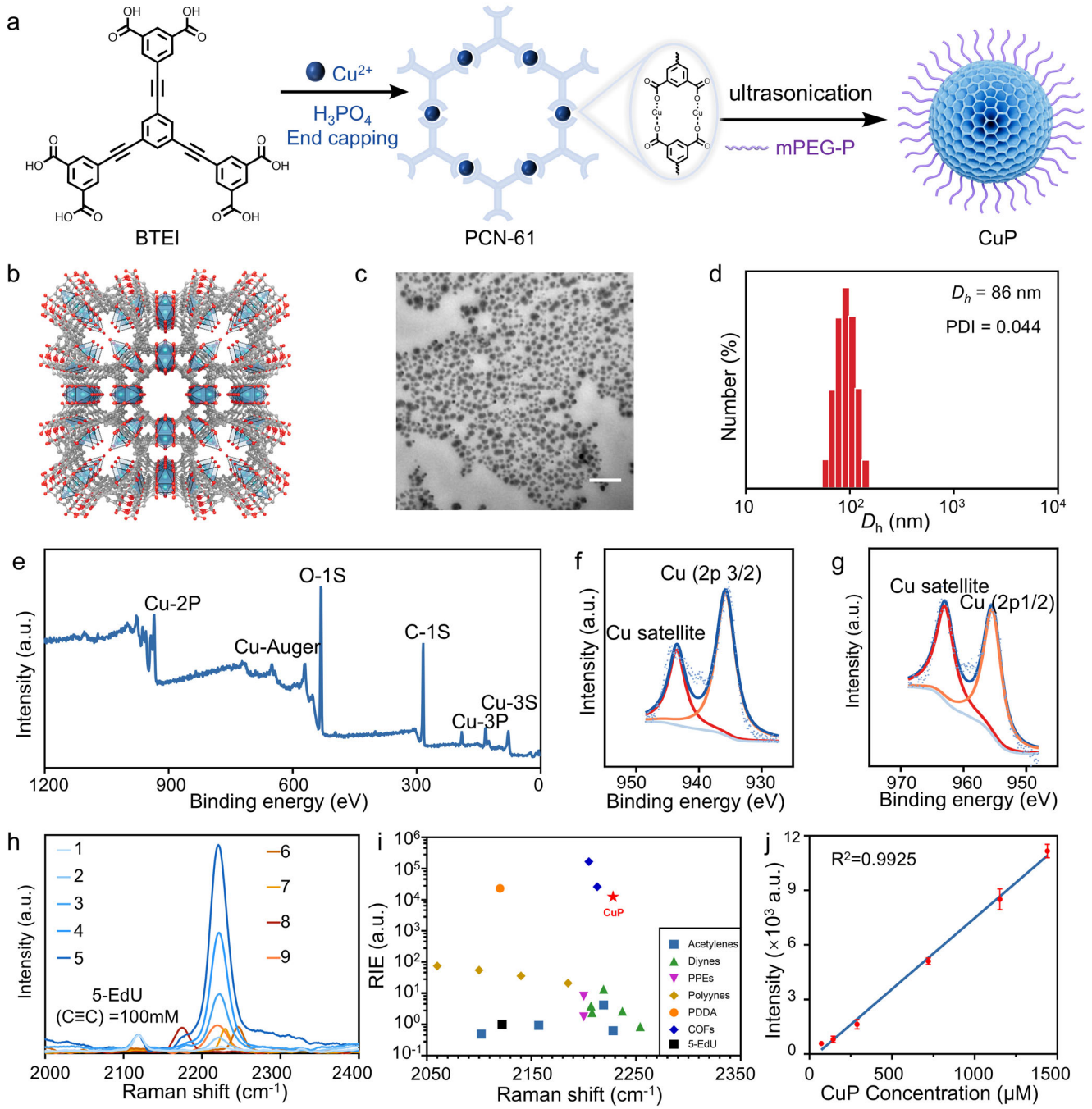


FIGURE 1 | The synthesis and characterization of CuP. (a) Schematic illustration of the synthesis procedure of CuP. (b) The structure of PCN-61 along the c-axis. (c) TEM image of CuP. Scale bar: 200 nm. (d) Size distribution of CuP measured by DLS. (e) Full XPS spectrum of CuP. (f, g) High-resolution Cu 2p XPS spectra of CuP. (h) Raman spectra of various bioorthogonal Raman probes. Samples 1–5 were prepared by mixing 3.5, 7, 56, 450, and 1800 μM CuP with 100 mM 5-EdU, respectively. Samples 6–9 were 100 mM small molecule alkyne-based Raman probes, including 5-bromovaleronitrile (6), benzonitrile (7), diphenyl azidophosphate (8), and BTEI (9). (i) RIE values of various bioorthogonal Raman probes (detailed data are presented in Table S2). (j) The calibration curve of Raman intensity at 2228 cm^{-1} as a function of CuP concentration (72 to 1440 μM) based on the C≡C bond in aqueous CuP solutions. Data are presented as mean ± SD from three replicate measurements at each concentration.

catalyst that converts H_2O_2 into more reactive intermediates. The literature has documented that Group VIII metal-based catalysts (typified by Fe and Ru) enable the oxidative cleavage of alkynes in organic solvents, whereas this reaction under physiological conditions (37 °C, aqueous solution) remains unexplored [41–43]. Given that Fe is an endogenous trace element and considering the stability requirements of the ligand in aqueous media, $[Fe(MeCN)_6(BF_4)_2]$ (Figures S11–S13) was selected as the catalyst [44]. Leveraging the ultrahigh surface area (> 3000 m^2/g) and large pores (> 1.8 nm) of CuP (Figure S14), $[Fe(MeCN)_6(BF_4)_2]$ was encapsulated via physical adsorption, yielding CuF with a ~40% loading efficiency (Table S3).

15213773, 0, Downloaded from https://onlinelibrary.wiley.com/doi/10.1002/anie.9809366 by National University Of Singapore, Wiley Online Library on [12/11/2026]. See the Terms and Conditions (https://onlinelibrary.wiley.com/terms-and-conditions) on Wiley Online Library for rules of use; OA articles are governed by the applicable Creative Commons License

Next, the catalyst-mediated degradation of CuF was evaluated using Raman spectroscopy (Figure 2a). As shown in Figure 2b, upon exposure to 100 μM H_2O_2, the alkynyl peak at 2228 cm^{-1} decreased progressively and was nearly undetectable by 48 h, directly confirming the oxidative cleavage of the alkynyl bonds in CuF. In contrast, the intensity of the alkynyl peak of CuF incubated in PBS alone (without H_2O_2) remained almost unchanged (Figure S10). This observation implies that oxidative cleavage of C≡C bonds within the ligand backbone might trigger the collapse of the Cu-MOFs with synchronous release of Cu^{2+}. To verify this hypothesis, we monitored the release of Cu^{2+} during the oxidation of CuF using inductively coupled plasma mass spectrometry (ICP-MS). As shown in Figure 2c, Cu^{2+} release from CuF within 16 h was less than 1% in the absence of H_2O_2, whereas substantial release was observed after incubation with H_2O_2 at concentrations relevant to the tumor microenvironment (10–100 μM). Moreover, the release rate increased with increasing H_2O_2 concentration, and approximately 72% of Cu^{2+} was released from CuF within 16 h in the presence of 100 μM H_2O_2. We further monitored the release of the Fe catalyst from CuF by ICP-MS under simulated serum and tumor conditions (Figure S15). Negligible Fe release occurred in simulated serum, whereas Fe was rapidly released under simulated tumor conditions along with the degradation of CuF. Taken together, both the Raman spectra and ICP-MS demonstrated that CuF remained stable under mild physiological conditions, while undergoing H_2O_2-triggered oxidation of C≡C bonds and releasing Cu^{2+}.

Given the causal relationship between alkyne degradation (measured by Raman spectroscopy) and Cu^{2+} release (measured by ICP-MS) (Figure 2d), we sought to establish a function to estimate the Cu^{2+} release percentage (Cu%) from Raman spectral data. To differentiate between two scenarios during imaging—the complete absence of CuF and the presence of CuF undergoing degradation—we adopted the aromatic ring peak at 1588 cm^{-1} (I_{1588}) as an internal reference. Using this reference, CuF is considered absent when both I_{1588} and I_{2228} (Raman signal at 2228 cm^{-1}) fall below the detection limit. Meanwhile, a decrease in the I_{2228}/I_{1588} ratio indicates the degradation of CuF. Based on these distinctions, we obtained the following fitting equation (Equation 1 and Figure 2d,e). Then, Equation (2) can be derived from Equation (1). Equation (2) directly establishes the relationship between Cu% and the I_{2228}/I_{1588} ratio. This relationship allows the Cu^{2+} release fraction to be estimated from Raman-detected CuF degradation. Overall, we have demonstrated that CuF degradation and the corresponding Cu^{2+} release could be assessed by ratiometric Raman imaging, representing a significant methodological advancement.

$$\frac{I_{2228}}{I_{1588}} = -2.89 \times 10^{-4}(Cu\%)^2 - 2.10 \times 10^{-4}(Cu\%) + 3.26 \quad (1)$$

$$Cu\% = \sqrt{376860.41 - 115600 \times \frac{I_{2228}}{I_{1588}}}/5.78 - 0.36 \quad (2)$$

To get further insights into the mechanism of catalyst-mediated oxidative cleavage of alkynyl moieties under physiological conditions, we characterized the reaction products in detail. First, we analyzed the oxidation products by nuclear magnetic resonance (NMR) spectroscopy. The disappearance of the alkynyl carbon peak in ^{13}C NMR spectrum (Figure S16) and the emergence of aldehyde proton peaks in ^{1}H NMR spectrum (Figure S17) validated the catalyst-mediated cleavage of alkyne bonds and the formation of aldehyde derivatives. Liquid chromatography-mass spectrometry (LC-MS) analysis further identified three primary oxidation products: benzene-1,3,5-tricarbaldehyde (BTH, *m/z* 163.0387, Figure 2f), 5-formylisophthalic acid (5FA, *m/z* 193.0132, Figure 2g), and benzene-1,3,5-tricarboxylic acid (BTA, *m/z* 209.0083, Figure 2h). Subsequently, BTH, 5FA, and BTA were isolated from the oxidation products by column chromatography, and their structures were unambiguously confirmed by ^{1}H NMR spectra (the insets in Figure 2f–h). To further validate the oxidation pathway, a model reaction was performed using 1-bromo-4-(phenylethynyl)benzene under identical catalytic conditions (Figure S18). Utilizing the characteristic bromine isotope peaks of the model molecule, ESI-MS identified two oxidation products: 4-bromobenzoic acid and 4-bromobenzaldehyde. This confirms that aromatic alkynes can be oxidized to aldehydes or carboxylic acids in an aqueous medium via $[Fe(MeCN)_6(BF_4)_2]$ catalysis.

The oxidative products of CuF identified above are consistent with those from hydroxyl radicals (•OH)-mediated oxidation of unsaturated hydrocarbons in organic solvents. We therefore hypothesize that the oxidation of CuF is mediated by hydroxyl radicals. To test this hypothesis, electron spin resonance (ESR) was employed to verify the presence of hydroxyl radicals during CuF oxidation in aqueous H_2O_2. Using 5,5-dimethyl-1-pyrroline N-oxide as a spin trap, a clear •OH signal was observed when CuF was incubated with 10 μM H_2O_2, whereas no radical signal was detected with catalyst-free CuP (Figure 2i). Quantitative fluorescence analysis using terephthalic acid further confirmed a significant increase in •OH generation for CuF (containing 1 μM $[Fe(MeCN)_6(BF_4)_2]$) compared with catalyst-free CuP (Figures 2j and S19). These results unequivocally establish the catalytic ability of $[Fe(MeCN)_6(BF_4)_2]$ to promote •OH production, thereby significantly facilitating the degradation of CuF.

Density functional theory calculations were then used to obtain the intermediates and Gibbs free-energy changes of oxidative alkyne cleavage with and without $[Fe(MeCN)_6(BF_4)_2]$ [45]. The Fe-catalyzed pathway exhibited a substantially lower initial free-energy barrier (60.6 $kJ \cdot mol^{-1}$, Figure 2n) than the uncatalyzed pathway (198.4 $kJ \cdot mol^{-1}$, Figure 2o). Moreover, the major intermediates along the proposed Fe-catalyzed pathway were markedly stabilized relative to those in the uncatalyzed reaction, supporting a more energetically favorable Fe-catalyzed pathway than the uncatalyzed reaction. This marked reduction of the kinetic barrier directly underpins the sensitive, catalyst-mediated degradation of CuF at pathophysiological levels of H_2O_2 (Figure S20).

The presence of free radicals, together with theoretical calculation results, implies that the central iron in $[Fe(MeCN)_6(BF_4)_2]$ may undergo valence state changes. This hypothesis was verified by XPS experiments. While iron in $[Fe(MeCN)_6(BF_4)_2]$ remained Fe(II) in PBS alone (Figure 2k), exposure to H_2O_2 led to the appearance of Fe(III) (Figure 2l). Specifically, in the presence of both H_2O_2 and CuP, a higher oxidation state (likely Fe(IV)) was observed (Figure 2m), analogous to intermediates in cytochrome P450 oxidase and biomimetic iron catalysts [46, 47]. This high-valent iron species is

15213773, 0, Downloaded from https://onlinelibrary.wiley.com/doi/10.1002/anie.98093366 by National University Of Singapore, Wiley Online Library on [12/11/2026]. See the Terms and Conditions (https://onlinelibrary.wiley.com/terms-and-conditions) on Wiley Online Library for rules of use; OA articles are governed by the applicable Creative Commons License

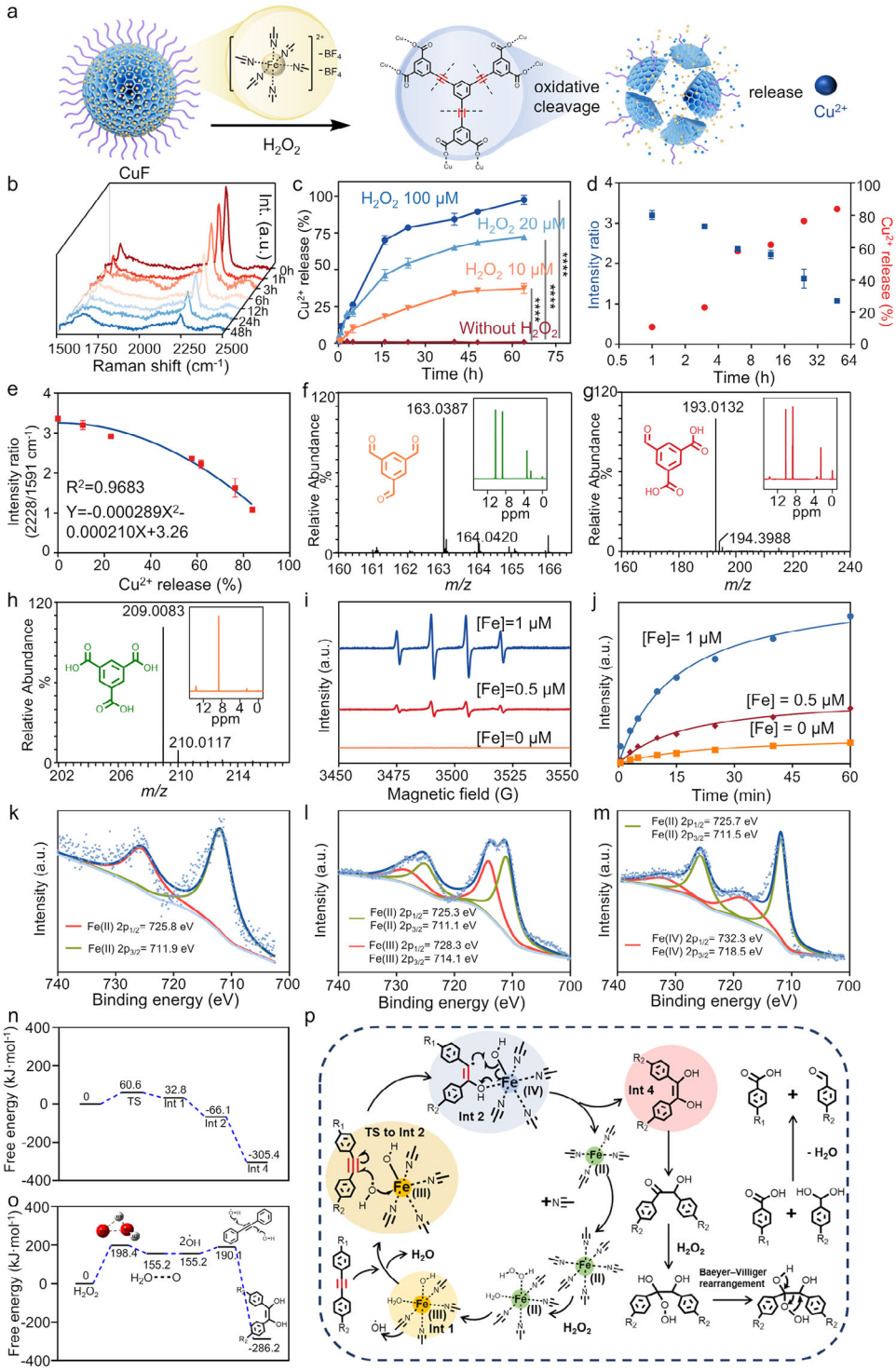


FIGURE 2 | Characterization of the oxidative degradation of CuF. (a) Schematic illustration of oxidative degradation process of CuF in the presence of H_2O_2. (b) Raman spectra of CuF after exposure to 100 μM H_2O_2 at different time points. (c) Release profile of Cu^{2+} from CuF in PBS (pH = 7.4) with or without H_2O_2 (10, 20, 100 μM) at 37 °C. Data are presented as mean ± SD (n = 3 replicate samples). Statistical significance was assessed using ordinary two-way ANOVA, followed by Dunnett's multiple-comparisons test comparing each group. (d) Time-dependent oxidative degradation of CuF in the presence of H_2O_2. Blue dots: Relative Raman intensity ratio of the alkyne peak to the aromatic ring peak (I_{2228} / I_{1588}); red dots: Cu^{2+} release percentage. (e) Fitting curve of the functional relationship between I_{2228} /I_{1588} and Cu% release. (f-h) MS and ^{1}H NMR spectra of the oxidation products: (f) BTH, (g) 5FA, and (h) BTA. (i) ESR spectra obtained upon 1 mM CuP addition of 10 μM H_2O_2 with [$Fe(MeCN)_6(BF_4)_2$] concentrations of 0, 0.5, and 1 μM. (j) Fluorescence intensity-time profiles of •OH in aqueous H_2O_2 solution with and without [$Fe(MeCN)_6(BF_4)_2$]. (k-m) High-resolution XPS spectra of 1 mM [$Fe(MeCN)_6(BF_4)_2$] reacted with: (k) PBS, (l) 2 mM H_2O_2, and (m) 2 mM H_2O_2 and 2 mM CuP (see Figure S11 for full XPS spectra). (n, o) Calculated Gibbs free energy profile of the intermediates and transition states involved in the proposed oxidative cleavage of the alkyne bond in the presence of [$Fe(MeCN)_6(BF_4)_2$] catalyst (n) or without catalyst (o). (p) Proposed mechanism for the catalytic oxidation of alkynyl groups in CuF.

15213773, 0, Downloaded from https://onlinelibrary.wiley.com/doi/10.1002/anie.98093366 by National University Of Singapore, Wiley Online Library on [12/11/2026]. See the Terms and Conditions (https://onlinelibrary.wiley.com/terms-and-conditions) on Wiley Online Library for rules of use; OA articles are governed by the applicable Creative Commons License

known to stabilize the unpaired electron of radical intermediates through electron delocalization [48].

Drawing on these results, we propose the following catalytic cycle (Figure 2p). Initially, Fe(II) loses two ligands and is then oxidized by H_2O_2 and release one hydroxyl radical, followed by η^2-coordination with the alkyne bond in the substrate to form the Fe(III)-centered intermediate (Int-1 and TS) [44]. This η^2 complex undergoes isomerization and oxidation, yielding the Fe(IV)-centered intermediate Int-2 [43]. Int-2 then undergoes reductive elimination, releasing the oxidation product (Int-4) and reducing iron back to Fe(II). Finally, acetonitrile ligands rebind to regenerate the catalyst. Meanwhile, the Int-4 undergoes enol-to-keto tautomerization to form a 1,2-diketone, which is subsequently hydrolyzed into a carboxylic acid and an aldehyde.

2.3 | Cuproptosis-Mediated Cytotoxicity of Cu-MOF Nanoparticles

Given the H_2O_2-responsive Cu^{2+} release capability of CuF, we next investigated its cuproptosis-mediated cytotoxicity in mouse breast cancer cells (4T1). It is well-known that breast cancer cells exhibit elevated ROS levels due to mitochondrial DNA mutations and metabolic reprogramming, which provide an effective trigger for inducing Cu^{2+} release from CuF in tumor cells (Figure S21) [26, 29, 49, 50]. First, the cellular uptake of CuF was investigated by confocal laser scanning microscopy (CLSM) and Raman imaging. As shown in Figure S22, CLSM images revealed that the fluorescence was clearly observed in tumor cells after incubation with CuF for 1.5 h, and the fluorescence intensity remained essentially unchanged up to 12 h, indicating effective internalization of CuF. Similarly, in Raman imaging, the characteristic signal of the alkynyl group (I_{2228}) prominently emerged in both 4T1 and L929 cells at 1.5 h, demonstrating that the internalization of CuF had already occurred (Figures 3a and S23). Moreover, in 4T1 cells, I_{2228} began to decline by 12 h and was largely diminished by 24 h (Figure 3b,c), whereas the intensities of the aromatic ring peaks (I_{1588}) remained essentially unchanged during this period (Figure 3a–c). By contrast, in L929 cells, the intensities of both I_{2228} and I_{1588}, as well as their intensity ratio, remained nearly unchanged at 12 and 24 h (Figure S23). This confirms the ROS-dependent oxidative cleavage of alkynyl bonds and degradation of CuF in 4T1 cells. Meanwhile, the stability observed in L929 cells excludes cellular extrusion as the cause of the diminished I_{2228} signal. Therefore, in contrast to CLSM observations, Raman imaging not only visualized the uptake of CuF but also revealed its intracellular degradation profile [51].

Next, we quantified the release of Cu^{2+} in 4T1 cells by integrating Raman spectroscopy with ICP-MS analysis. As shown in Figure S24, cellular copper accumulated over time, with approximately half of the encapsulated Cu^{2+} released in responsive manner from CuF after incubation for 8 h. Importantly, at this time point, less than 15% of the released copper remained as free ions, while over 80% complexed with intracellular proteins, which is a prerequisite for inducing cuproptosis [1, 52]. Control experiments in L929 cells showed a comparable CuF internalization rate, while the free Cu^{2+} concentration remained low throughout the observation period, and most internalized CuF remained undegraded, confirming the selective degradation of CuF (Figure S25). Additionally, at 8 h post-incubation, the cellular copper concentration was approximately 100-fold higher in the CuF treatment group than in the PBS-treated control group (Figure S26), indicating significant intracellular copper overload after CuF treatment.

In light of the effective internalization of CuF and release of Cu^{2+}, we then evaluated the cytotoxicity of CuF against 4T1 cells with varying catalyst loadings (Figure S27). Neither catalyst-free CuP nor $[Fe(MeCN)_6(BF_4)_2]$ alone exhibited significant cytotoxicity. The cytotoxicity of CuF increased dose-dependently with catalyst loading up to 3.8 mol%, beyond which it plateaued, due to saturation of the intracellular H_2O_2-driven oxidation kinetics. Thus, CuF containing 3.8 mol% $[Fe(MeCN)_6(BF_4)_2]$ (based on alkynyl equivalent) was selected for subsequent studies. Notably, CuF exhibited an IC_{50} of 72 μM (based on Cu^{2+} concentration), which was more cytotoxic than free $CuCl_2$ (IC_{50} = 128.7 μM, Figure S28). In addition, CuF also exhibited potent cytotoxicity against other tumor cells with elevated intracellular H_2O_2 levels, including B16 (melanoma, IC_{50} = 41 μM) and CT26 (colon adenocarcinoma, IC_{50} = 40 μM), while being less cytotoxic to normal cells, including L929 (fibroblast cells, IC_{50} = 216 μM) and HUVEC (endothelial cells, IC_{50} = 432 μM) (Figure 3d). These results demonstrate that CuF possesses selective cytotoxicity toward tumor cells with elevated H_2O_2 levels.

To explore the underlying mechanism of CuF-induced cytotoxicity, we quantitatively analyzed the expression of cuproptosis-related proteins in 4T1 cells using Western blot assays (Figures 3e and S29–S31). Treatment with CuF (9 or 18 μM) induced significant oligomerization of dihydrolipoamide S-acetyltransferase (DLAT) and downregulated expression of lipoyl synthase (LIAS) and ferredoxin 1 (FDX-1). In contrast, neither CuP nor catalyst alone elicited these changes. Immunofluorescence imaging further corroborated these findings, visualizing distinct DLAT aggregation and reduced LIAS expression in CuF-treated groups (Figures 3g and S32). We further performed a copper-chelation rescue experiment, in which cotreatment with tetrathiomolybdate (TTM), a copper chelator [1, 53], markedly alleviated CuF-induced cytotoxicity, restoring cell viability from approximately 12% to 70% at 96 μM CuF (Figure S33). Together, these results demonstrate that CuF robustly triggers the cuproptosis pathway in 4T1 cells.

In addition to the cytotoxicity induced by Cu^{2+}, we further investigated whether the oxidative degradation products of CuF (BTH, 5FA, and BTA) contribute to the cytotoxicity. As seen in Figures 3f and S34, BTH, 5FA, and BTA alone exhibited low cytotoxicity (cell viability > 80% at 144 μM), whereas the degradation product–Cu^{2+} combinations displayed enhanced cytotoxicity. Bliss independence analysis supported synergistic interactions for most of the tested degradation product–Cu^{2+} combinations (Figure S35). Synchronous-asynchronous treatment experiments ruled out extracellular chelation-facilitated uptake of Cu^{2+} (Figure S36), confirming an intracellular synergistic mechanism. To further elucidate the synergistic mechanism, we incubated the oxidative degradation products with DLAT. Gel electrophoresis revealed the decreased monomeric DLAT (70 kDa) and the appearance of a 140 kDa band (Figures 3h and S37), suggesting that these degradation products may destabilize DLAT and induce its denaturation or aggregation.

15213773, 0, Downloaded from https://onlinelibrary.wiley.com/doi/10.1002/anie.9809366 by National University Of Singapore, Wiley Online Library on [12/11/2026]. See the Terms and Conditions (https://onlinelibrary.wiley.com/terms-and-conditions) on Wiley Online Library for rules of use; OA articles are governed by the applicable Creative Commons License

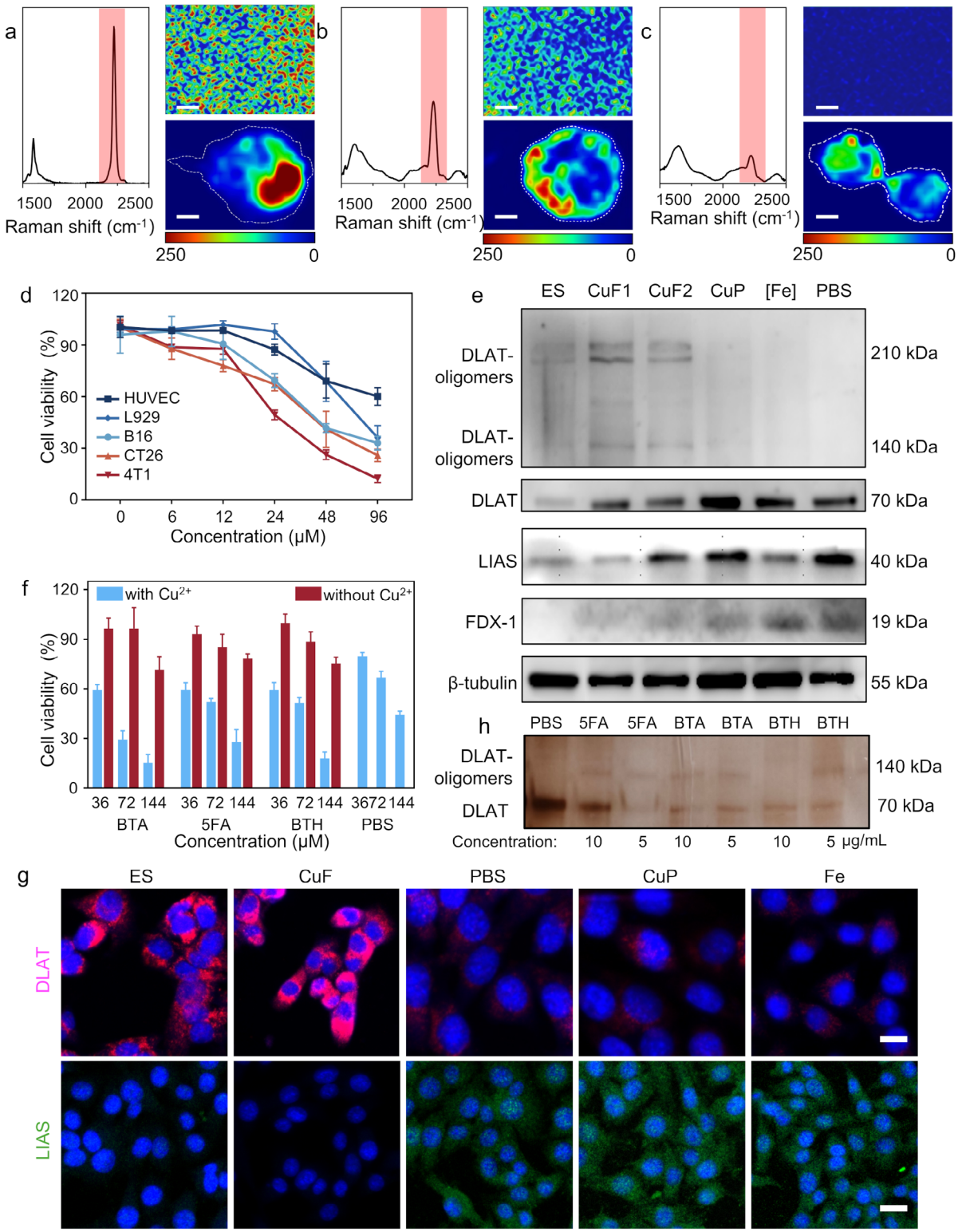


FIGURE 3 | In vitro anticancer activity and mechanism of CuF. (a–c) Raman imaging of 4T1 cells treated with CuF (36 μM) for (a) 1.5, (b) 12, and (c) 24 h, monitored at 2228 cm^{-1}. Scale bars: upper, 60 μm; lower, 3 μm. (d) Cytotoxicity of CuF against different cell lines. (e) Western blot analysis of DLAT, LIAS, and FDX-1 in 4T1 cells after 24 h of treatment. Uncropped Western blot images are provided in Figures S29–S31. (f) Cytotoxicity of three oxidation products (PBS: control groups were treated with PBS instead) against 4T1 cells, with and without equivalent amount of $CuCl_2$. (g) Immunofluorescence staining of DLAT (red) and LIAS (green) in 4T1 cells under various treatments for 12 h. Scale bar: 50 μm. (h) Silver-stained SDS-PAGE of 10 μg/mL DLAT after co-incubation with three oxidative degradation products for 12 h. Uncropped gel images are provided in Figure S37. Annotations for the abbreviations used in (e) and (g): ES: 18 μM elesclomol + 18 μM $CuCl_2$; CuF and CuF1: 18 μM CuF; CuF2: 9 μM CuF; PBS: PBS solution (pH 7.4); CuP: 18 μM CuP; Fe: 18 μM $[Fe(MeCN)_6(BF4)_2]$.

15213773, 0, Downloaded from https://onlinelibrary.wiley.com/doi/10.1002/anie.9809366 by National University Of Singapore, Wiley Online Library on [12/11/2026]. See the Terms and Conditions (https://onlinelibrary.wiley.com/terms-and-conditions) on Wiley Online Library for rules of use; OA articles are governed by the applicable Creative Commons License

2.4 | RNA Transcriptomics Validation of CuF-Induced Cuproptosis of 4T1 Cells

RNA-sequencing (RNA-seq) was performed to gain deeper insights into the transcriptional response of 4T1 cells to CuF treatment. As shown in Figure 4a, the heatmap of differentially expressed genes (DEGs) reveals distinct transcriptional profiles across samples with or without CuF treatment. DEGs were identified using thresholds of $|\log_{1.5}\text{fold change (FC)}| > 1$ and false discovery rate (FDR, adjusted p-value) < 0.05, as visualized in the volcano plot (Figure 4b). This analysis identified 538 significantly upregulated genes and 1,618 significantly downregulated genes. Notably, key genes related to TCA cycle and cuproptosis were prominently altered, including significant downregulation of *Dlat, Fdx1*, lipoyltransferase 1 (*Lipt1*), pyruvate dehydrogenase E1 subunit alpha 1 (*Pdha1*), and dihydrolipoamide dehydrogenase (*Dld*) (highlighted in blue) and marked upregulation of metal regulatory transcription factor 1 (*Mtf1*) and cyclin-dependent kinase inhibitor 2D (*Cdkn2d*) (highlighted in red). These genes are well-established biomarkers of cuproptosis [1], underscoring the specific induction of this cell death pathway by CuF.

Gene Ontology (GO) enrichment analysis revealed that CuF treatment predominantly altered gene distributions across the three GO domains: Biological Process (blue terms), Molecular Function (red terms), and Cellular Component (green terms, Figure 4c). Kyoto Encyclopedia of Genes and Genomes (KEGG) pathway analysis further identified notable enrichment in processes including C5-branched dibasic acid metabolism, mineral absorption, mitophagy, and glutathione metabolism, all of which were mechanistically linked to cuproptosis (Figure 4d). Supporting these findings, gene set enrichment analysis (GSEA) revealed a significant enrichment of mitophagy and mineral absorption pathway in CuF-treated cells (Figure 4e). This provides direct mechanistic evidence that CuF disrupts lipoylation, leading to DLAT oligomerization (as observed in prior experiments) and further confirming the induction of cuproptosis.

Based on the integrated evidence from prior experiments, we propose the following mechanism by which CuF disrupts the TCA cycle and induces cuproptosis (Figure 4f). CuF elevates the concentration of intracellular Cu^{2+}, which undergoes FDX-1/GSH-mediated reduction to Cu^{+}. This process leads to downregulation of FDX1 and perturbation of glutathione metabolism. As the core component (E2 subunit) of the pyruvate dehydrogenase complex, DLAT requires lipoylation to exert its normal function. The lipoylation process requires coordinated regulation by LIPT1, DLD, LIAS, and FDX-1, all of which are downregulated under copper overload conditions. Additionally, Cu^{+} reacts with the disulfide bonds in lipoylated DLAT, inducing its oligomerization and functional inactivation. This ultimately inhibits acetyl-CoA production, which further disrupts the TCA cycle and triggers cuproptosis.

2.5 | In Vivo Anticancer Activity of CuF

Having verified that CuF can trigger cuproptosis in cellular assays, we further evaluated its antitumor efficacy in 4T1 tumor-bearing mice. First, we performed pharmacokinetic experiments by leveraging the intrinsic Raman signal of CuF. To account for matrix-induced noise and bias, we established corresponding matrix-matched calibration curves using tumor tissue homogenates (Figure S38). The Raman response of CuP retained good linearity in the tumor matrix, although the limit of quantification increased owing to the biological background. Accordingly, measurements below the limit of quantification were excluded from subsequent analyses. After intravenous administration, blood samples were collected at designed time points, and plasma drug concentrations were subsequently quantified by Raman spectroscopy based on the established standard curve (Figure S39a). As shown in Figure S39b, CuF displayed a relatively long blood circulation half-life ($t_{1/2}$) of 29.5 ± 8.6 h. More importantly, the Raman estimate based on Equation (2) revealed that less than 5% of the encapsulated copper was released during circulation, highlighting its stability and minimal off-target leakage, a key feature that reduces systemic copper toxicity. We further used ICP-MS to examine the time-dependent biodistribution of Cu and Fe following CuF administration (Figure S40). Cu levels in the blood, major organs, and tumors increased rapidly after administration, peaked at 1 h, and subsequently declined, with the most pronounced increase observed in tumors. In contrast, total Fe levels exhibited only modest fluctuations. These results indicate that CuF effectively delivers Cu to tumors without causing substantial Fe accumulation.

Following the pharmacokinetic study, we further investigated the accumulation and degradation-mediated release behavior of CuF in tumor tissues via Raman spectroscopy. At 0.5, 1, 3, 6, and 12 h after intravenous injection of 9 mg/kg CuF or CuP, tumor sections were analyzed by mapping the characteristic peaks at 2228 and 1588 cm^{-1} (Figure 5a). The distributions of CuF and CuP (Figures 5b,c and S41) were visualized via the alkyne signal (I_{2228}), with tumor regions histologically confirmed by hematoxylin and eosin (H&E) staining. In addition, the degradation and Cu^{2+} release percentage of CuF or CuP in each section were estimated using a heatmap derived from the I_{2228}/ I_{1588} ratio and the calibrated Equation 2. As revealed by the distribution of CuF/CuP and H&E staining of the corresponding tissue regions, both CuF and CuP accumulated in tumors within 1 h and showed clear tumor-to-normal tissue contrast by 3 h, indicating effective accumulation of both agents in tumors. Meanwhile, by analyzing the heatmap data, we observed that in CuF-treated tumors, I_{2228} decreased markedly by 6 h, while the I_{1588} remained relatively strong until 12 h, indicating the effective degradation of CuF and the prolonged retention of oxidative products (Figure 5b). This spatiotemporally resolved visualization of tumor sections provides evidence for the catalyst-mediated, H_2O_2-induced degradation of CuF and its subsequent Cu^{2+} release within tumors. On the contrary, in CuP-treated tumors, no obvious degradation of CuP was observed. The Raman-estimated mean intratumoral Cu^{2+} release percentage at 12 h imaging was approximately 90.3% for the CuF group and merely 9.6% for the CuP group. This not only verified the indispensable role of the catalyst in CuF, but also demonstrated that CuP possesses tumor imaging capability, highlighting its potential utility as a high-contrast diagnostic probe for tumor delineation and intraoperative guidance (Figure S42). Ex vivo Raman imaging of organs at 12 h demonstrated minimal off-target accumulation of CuF (Figure S43), corroborating its favorable safety profile. Similarly, we evaluated the maximum tolerated dose (MTD) of CuF, which was nearly 20-fold higher

15213773, 0, Downloaded from https://onlinelibrary.wiley.com/doi/10.1002/anie.98093366 by National University Of Singapore, Wiley Online Library on [12/11/2026]. See the Terms and Conditions (https://onlinelibrary.wiley.com/terms-and-conditions) on Wiley Online Library for rules of use; OA articles are governed by the applicable Creative Commons License

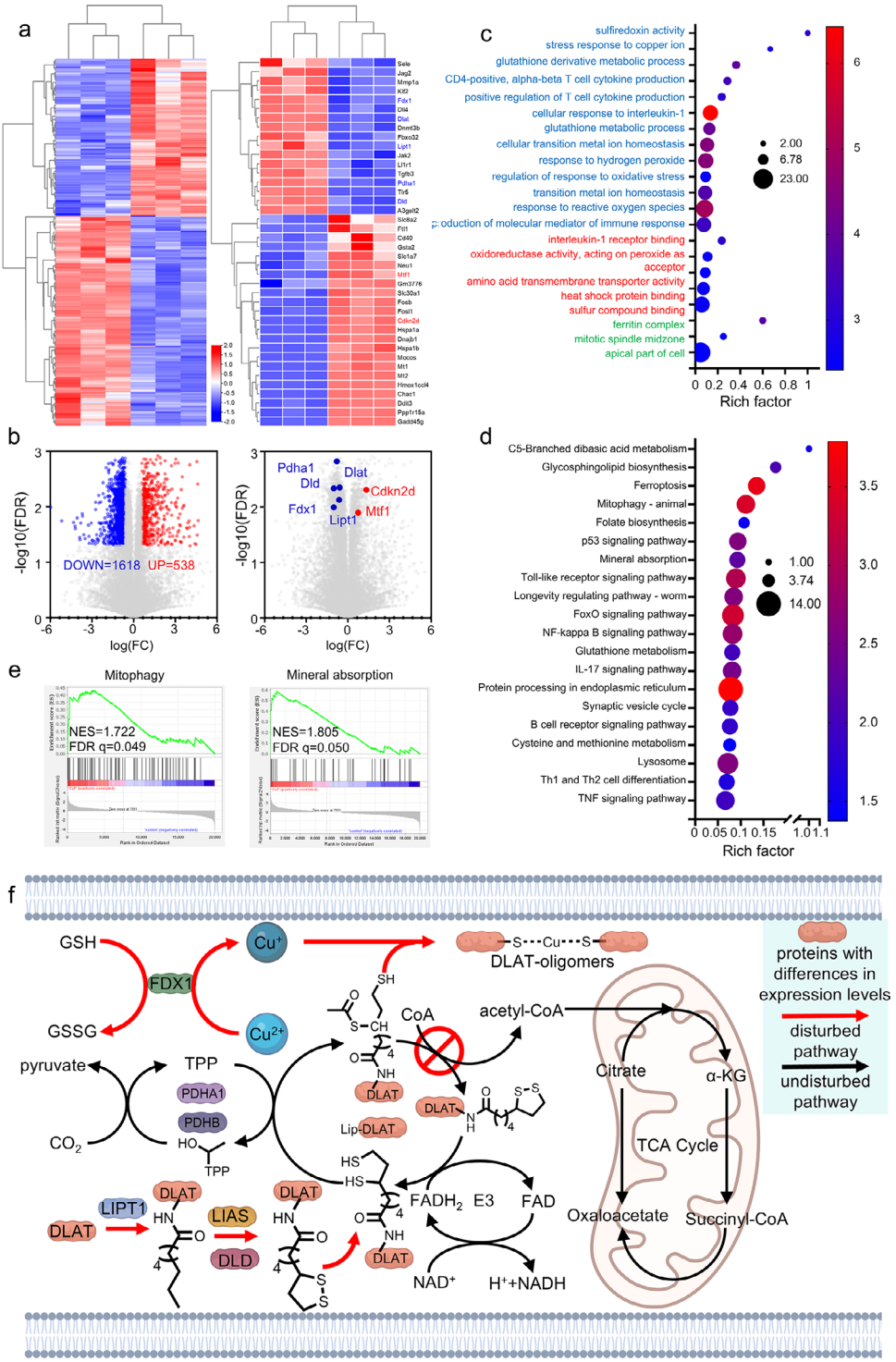


FIGURE 4 | RNA-seq analysis of 4T1 cells treated with CuF. (a) Cluster heatmap showing all DEGs (left) and cuproptosis-related DEGs (right) between CuF (18 μM) groups compared to the PBS group, red labeled: key genes with high expression blue labeled: key genes with low expression. (b) Volcano plot showing the DEGs in 4T1 Cells treated with CuF (18 μM) for 24 h, Standard: $|\log_{1.5}FC| > 1$; q value <0.05. (c) GO enrichment analysis from CuF group as compared with the control group. (d) KEGG enrichment analysis from CuF group as compared with the control group. (e) GSEA revealing positive enrichment of CuF-altered genes in various pathways. ES: enrichment score. NES: normalized enrichment score. (f) Cuproptosis-related pathways and the upstream proteins of TCA cycle disturbed by them. Changes verified by transcriptomic results have been highlighted. Protein abbreviations and full names are listed in Table S4.

15213773, 0, Downloaded from https://onlinelibrary.wiley.com/doi/10.1002/anie.98093366 by National University Of Singapore, Wiley Online Library on [12/11/2026]. See the Terms and Conditions (https://onlinelibrary.wiley.com/terms-and-conditions) on Wiley Online Library for rules of use; OA articles are governed by the applicable Creative Commons License

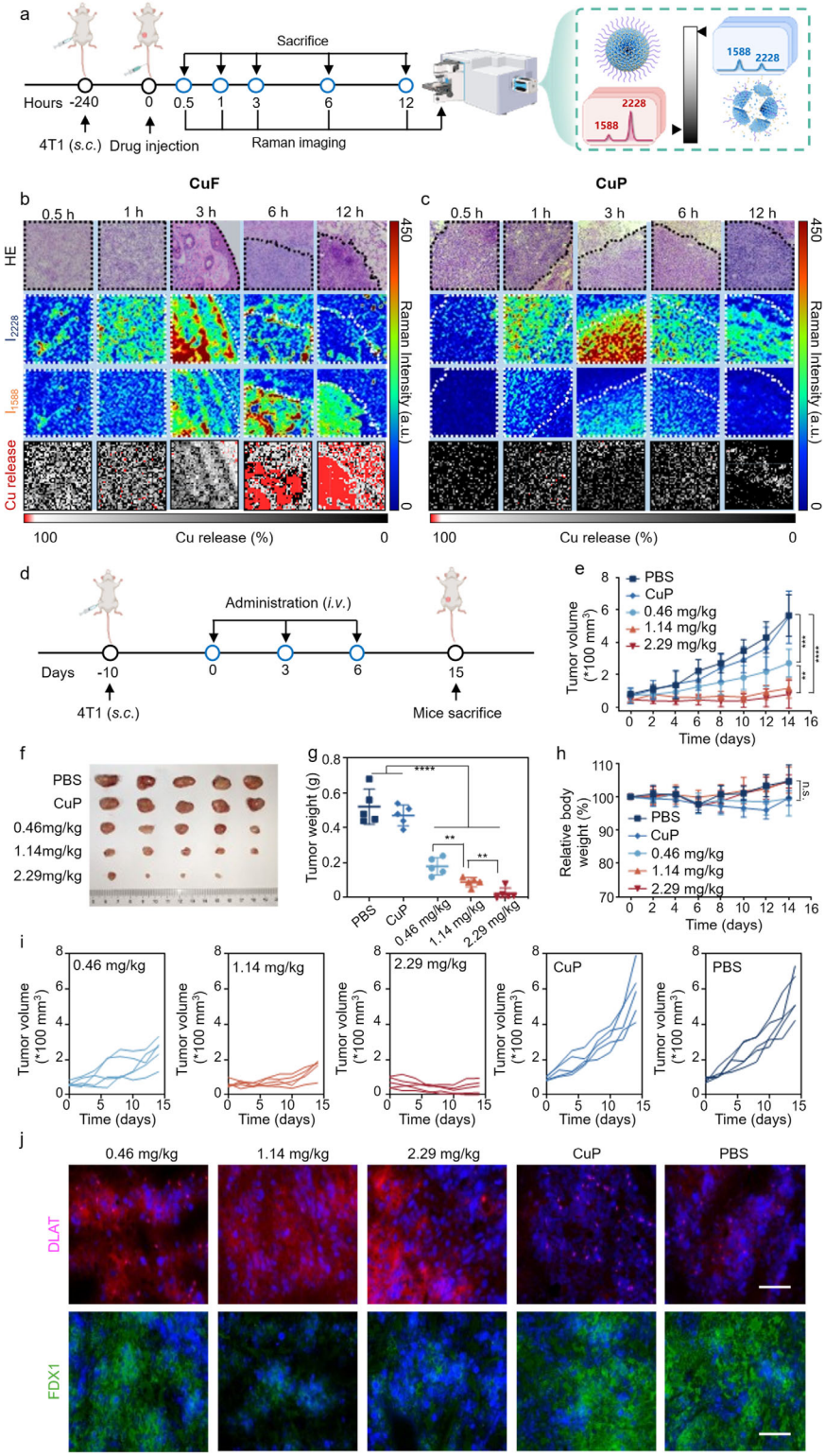


FIGURE 5 | In vivo pharmacokinetics, tissue-section Raman analysis, and antitumor activity of CuF. (a) Establishment process and Raman imaging schedule of the 4T1 murine tumor model. (b, c) H&E and Raman imaging of tumor and surrounding tissue sections at 0.5–12 h after intravenous administration of CuF and CuP, and heatmap of the Raman-estimated Cu^{2+} release fraction derived from the matrix-calibrated I_{2228}/I_{1588} model. Corresponding tissue sections from PBS-treated mice are shown in Figure S41. (d) Schematic of the 4T1 murine tumor model establishment and therapeutic regimen. (e) Tumor growth curves under different treatments ($n = 5$). (f) Images of tumors from each group at the end of treatment. (g) Weights of tumors from each group at the end of treatment. (h) Relative body weight changes of mice after different treatments. (i) Individual tumor growth curves of all treatment groups. (j) Immunofluorescence (DLAT, FDX-1) staining of tumor tissues after different treatments. Scale bar = 100 μm. Detailed statistical analysis of Figure 5 is provided in the Supporting Information.

15213773, 0, Downloaded from https://onlinelibrary.wiley.com/doi/10.1002/anie.9809366 by National University Of Singapore, Wiley Online Library on [12/11/2026]. See the Terms and Conditions (https://onlinelibrary.wiley.com/terms-and-conditions) on Wiley Online Library for rules of use; OA articles are governed by the applicable Creative Commons License

than that of $CuCl_2$, further confirming its favorable safety profile (Figure S44).

The antitumor efficacy of CuF was then evaluated in a 4T1 tumor-bearing BALB/c mouse model (Figure 5d). Once subcutaneous tumors reached 60–80 mm^3 in volume, the mice were randomly allocated into five groups (n = 5 per group). Two negative control groups received intravenous injections of PBS and CuP (2.29 mg/kg, Cu equivalent) respectively via the tail vein every 3 days for a total of three administrations, while the experimental groups were treated with CuF at escalating doses of 0.46, 1.14, and 2.29 mg/kg (Cu equivalent) under the same administration schedule. Tumors in the PBS and CuP groups grew rapidly, reaching an average volume of approximately 550 mm^3 within 14 days (Figure 5e–g). In contrast, all CuF-treated groups exhibited significant tumor suppression. Administration of 0.46, 1.14, and 2.29 mg/kg CuF resulted in tumor inhibition rates of 65%, 80%, and 91%, respectively (Figure 5i). Only minor body weight fluctuations were observed across all groups throughout the treatment, indicating minimal systemic toxicity (Figure 5h). Immunofluorescence analyses of tumor sections provided mechanistic insight (Figures 5j and S45). CuF-treated tumors showed pronounced DLAT oligomerization and downregulated FDX-1 expression, confirming the induction of cuproptosis in vivo. Meanwhile, H&E staining of tumor sections from groups treated with different concentrations of CuF revealed various degrees of cell death compared with the negative control groups (Figure S46).

Systemic safety was assessed via serum biochemistry, urine biochemistry, and histopathological examination. Renal (urea, creatinine, uric acid) and hepatic (alanine aminotransferase, aspartate aminotransferase, and alkaline phosphatase) markers in CuF-treated mice remained within normal physiological ranges and had no statistically significant difference from the PBS control (Figure S47). H&E staining of major organs revealed no noticeable morphological alterations (Figure S46). Together, these findings demonstrate the favorable safety profile and low systemic toxicity of CuF in vivo.

3 | Conclusion

In summary, we have developed a Raman self-tracking nanoplatform named CuF for cuproptosis-mediated tumor therapy. CuF was synthesized by using chelating Cu^{2+} with an alkynyl-rich ligand (BTEI), followed by PEGylation to form stable nanoparticles, and encapsulating an iron-based catalyst $[Fe(MeCN)_6(BF_4)_2]$ to trigger oxidative degradation. The obtained CuF exhibited high stability under normal physiological conditions, while it could be degraded through the catalytic oxidative cleavage of alkynyl bonds in the presence of H_2O_2. The catalytic oxidative degradation of CuF caused the release of Cu^{2+}, leading to intracellular copper overload and subsequently inducing cuproptosis in 4T1 cells. Meanwhile, the aldehydes and acids generated during alkynyl oxidation also synergistically enhanced cuproptosis. Consequently, CuF exhibited remarkable antitumor efficacy in a 4T1 breast cancer model with minimal systemic toxicity. Furthermore, by leveraging the intrinsic enhanced Raman signal of CuF and correlating the Raman intensity ratio (I_{2228}/ I_{1588}) with the Cu^{2+} release percentage, we achieved label-free, spatiotemporally resolved visualization of CuF fate from cellular uptake to intratumoral activation through ex vivo Raman imaging. Overall, our results open up new directions for the design and preparation of oxidation-responsive MOF-based nanoplatforms with built-in Raman self-tracking capability. Moreover, we believe this strategy sheds new light on the development of next-generation metal-based anticancer agents.

Author Contributions

Yujie Duan: writing – original draft, methodology, investigation, conceptualization, formal analysis. **Ying Bao:** funding acquisition, writing – review and editing, data curation, validation, formal analysis. **Ziwen Gao:** data curation, visualization, writing – review and editing. **Xidong He:** methodology, writing – review and editing, validation. **Xinming Liu:** validation, visualization. **Hao Wang:** writing – review and editing, supervision, methodology, funding acquisition. **Chunsheng Xiao:** resources, project administration, writing – review and editing, methodology, conceptualization, supervision. **Xuesi Chen:** supervision, resources, writing – review and editing, project administration.

Acknowledgments

The authors acknowledge the financial support by the National Natural Science Foundation of China (52473325, 52503211), and the Jilin Province Science and Technology Development Programs (20250206037ZP).

Conflicts of Interest

Hao Wang, Yujie Duan, Ying Bao, Chunsheng Xiao, and Xuesi Chen are inventors on a Chinese patent application (CN202510752521.0) related to the work described in this manuscript and filed by the Changchun Institute of Applied Chemistry, Chinese Academy of Sciences. The other authors declare no conflicts of interest.

Data Availability Statement

The data that support the findings of this study are available in the supplementary material of this article.

References

1. P. Tsvetkov, S. Coy, B. Petrova, et al., "Copper Induces Cell Death by Targeting Lipoylated TCA Cycle Proteins," *Science* 375 (2022): 1254–1261, https://doi.org/10.1126/science.abf0529.

2. P. Zheng, C. Zhou, L. Lu, B. Liu, and Y. Ding, "Elesclomol: A Copper Ionophore Targeting Mitochondrial Metabolism for Cancer Therapy," *Journal of Experimental & Clinical Cancer Research* 41 (2022): 271, https://doi.org/10.1186/s13046-022-02485-0.

3. P. Zhao, H. Wang, H. Zhao, et al., "Tumor Microenvironment-Reprogrammable CpG-Templated Copper Sulfide Loaded with Disulfiram for Sensitized Cuproptosis Immunotherapy," *Chemical Engineering Journal* 487 (2024): 150524, https://doi.org/10.1016/j.cej.2024.150524.

4. Y. Lu, Q. Pan, W. Gao, et al., "Leveraging Disulfiram to Treat Cancer: Mechanisms of Action, Delivery Strategies, and Treatment Regimens," *Biomaterials* 281 (2022): 121335, https://doi.org/10.1016/j.biomaterials.2021.121335.

5. G. Kismali, F. Emen, T. Yesilkaynak, et al., "The Cell Death Pathway Induced by Metal Halide Complexes of Pyridine and Derivative Ligands in Hepatocellular Carcinoma Cells–Necrosis or Apoptosis?" *European Review for Medical & Pharmacological Sciences* 16 (2012): 1001.

6. A. Chaudhary, A. Kumar, A. Ankit, and R. G. Singh, "Discovery of Cu(II)-Dipyridophenazine Complex for Synergistic Cuproptosis/Chemodynamic Therapy via Disrupting the Tricarboxylic Acid (TCA) Cycle in Metastatic TNBC," *Small* 21 (2025): 2504554, https://doi.org/10.1002/smll.202504554.

15213773, 0, Downloaded from https://onlinelibrary.wiley.com/doi/10.1002/anie.9809366 by National University Of Singapore, Wiley Online Library on [12/11/2026]. See the Terms and Conditions (https://onlinelibrary.wiley.com/terms-and-conditions) on Wiley Online Library for rules of use; OA articles are governed by the applicable Creative Commons License

7. D. Tang, G. Kroemer, and R. Kang, "Targeting Cuproplasia and Cuproptosis in Cancer," *Nature Reviews Clinical Oncology* 21 (2024): 370–388, https://doi.org/10.1038/s41571-024-00876-0.

8. F. Hu, J. Huang, T. Bing, et al., "Stimulus-Responsive Copper Complex Nanoparticles Induce Cuproptosis for Augmented Cancer Immunotherapy," *Advanced Science* 11 (2024): 2309388.

9. G. He, Y. Pan, F. Zeng, et al., "Microfluidic Synthesis of CuH Nanoparticles for Antitumor Therapy Through Hydrogen-Enhanced Apoptosis and Cuproptosis," *ACS Nano* 18 (2024): 9031–9042, https://doi.org/10.1021/acsnano.3c12796.

10. B. Guo, F. Yang, L. Zhang, et al., "Cuproptosis Induced by ROS Responsive Nanoparticles With Elesclomol and Copper Combined With αPD-L1 for Enhanced Cancer Immunotherapy," *Advanced Materials* 35 (2023): 2212267, https://doi.org/10.1002/adma.202212267.

11. X. Han, X. Zhang, Z. Liu, et al., "Copper-Based Nanotubes That Enhance Starvation Therapy Through Cuproptosis for Synergistic Cancer Treatment," *Advanced Science* 12 (2025): e04121, https://doi.org/10.1002/advs.202504121.

12. L. Qiao, G. Zhu, T. Jiang, et al., "Self-Destructive Copper Carriers Induce Pyroptosis and Cuproptosis for Efficient Tumor Immunotherapy Against Dormant and Recurrent Tumors," *Advanced Materials* 36 (2024): 2308241, https://doi.org/10.1002/adma.202308241.

13. C. Zhao, X. Tang, X. Chen, and Z. Jiang, "Multifaceted Carbonized Metal–Organic Frameworks Synergize with Immune Checkpoint Inhibitors for Precision and Augmented Cuproptosis Cancer Therapy," *ACS Nano* 18 (2024): 17852–17868, https://doi.org/10.1021/acsnano.4c04022.

14. J. Bao, J. Wang, S. Chen, et al., "Coordination Self-Assembled AuTPyP-Cu Metal–Organic Framework Nanosheets With pH/Ultrasound Dual-Responsiveness for Synergistically Triggering Cuproptosis-Augmented Chemotherapy," *ACS Nano* 18 (2024): 9100–9113, https://doi.org/10.1021/acsnano.3c13225.

15. Y. Bao, Z. Gao, Y. Yan, et al., "Covalent Organic Framework-Based Ultrasensitive Bioorthogonal Raman Probes for In Vivo Detection of Bone Crack," *Advanced Functional Materials* 36 (2026): e22613, https://doi.org/10.1002/adfm.202522613.

16. S. S.-Y. Chui, S. M.-F. Lo, J. P. Charmant, A. G. Orpen, and I. D. Williams, "A Chemically Functionalizable Nanoporous Material $[Cu_3(TMA)_2\,(H2O)_3]n$," *Science* 283 (1999): 1148.

17. H. Li, M. Eddaoudi, M. O'Keeffe, and O. M. Yaghi, "Design and Synthesis of an Exceptionally Stable and Highly Porous Metal-Organic Framework," *Nature* 402 (1999): 276–279, https://doi.org/10.1038/46248.

18. M. Ding, X. Cai, and H.-L. Jiang, "Improving MOF Stability: Approaches and Applications," *Chemical Science* 10 (2019): 10209–10230, https://doi.org/10.1039/C9SC03916C.

19. D. Zhao, D. Yuan, D. Sun, and H.-C. Zhou, "Stabilization of Metal–Organic Frameworks with High Surface Areas by the Incorporation of Mesocavities with Microwindows," *Journal of the American Chemical Society* 131 (2009): 9186–9188, https://doi.org/10.1021/ja901109t.

20. R. Haldar, A. Ghosh, and T. K. Maji, "Charge Transfer in Metal–Organic Frameworks," *Chemical Communications* 59 (2023): 1569–1588, https://doi.org/10.1039/D2CC05522H.

21. L. Wang, A. Sarkar, G. L. Grocke, et al., "Broad Electronic Modulation of Two-Dimensional Metal–Organic Frameworks over Four Distinct Redox States," *Journal of the American Chemical Society* 145 (2023): 8486–8497, https://doi.org/10.1021/jacs.3c00495.

22. L. Shupletsov, S. Topal, A. Schieck, et al., "Linker Conformation Controls Oxidation Potentials and Electrochromism in Highly Stable Zr-Based Metal–Organic Frameworks," *Journal of the American Chemical Society* 146 (2024): 25477–25489, https://doi.org/10.1021/jacs.4c04653.

23. Y. Yao, X. Zhang, Y. Cao, L. Liu, Y. Zhang, and S. Zhang, "Single-Site Pd Regulated by π–π Stacking for High-Selectivity Cyclopropanation Reaction," *Journal of the American Chemical Society* 146 (2024): 31053–31061, https://doi.org/10.1021/jacs.4c10860.

24. M. Kawasaki and T. Sato, "Direct Voltammetric Observation of Reversible and Irreversible Oxidations of Two-Dimensional J-Aggregates of Cyanine Dye," *Journal of Physical Chemistry B* 105 (2001): 796–803, https://doi.org/10.1021/jp002309a.

25. J. Li and S. Ott, "The Molecular Nature of Redox-Conductive Metal–Organic Frameworks," *Accounts of Chemical Research* 57 (2024): 2836–2846, https://doi.org/10.1021/acs.accounts.4c00430.

26. F. Tas, H. Hansel, A. Belce, et al., "Oxidative Stress in Breast Cancer," *Medical Oncology* 22 (2005): 011–016, https://doi.org/10.1385/MO:22:1:011.

27. W. Zai, L. Kang, T. Dong, et al., "*E. coli* Membrane Vesicles as a Catalase Carrier for Long-Term Tumor Hypoxia Relief to Enhance Radiotherapy," *ACS Nano* 15 (2021): 15381–15394, https://doi.org/10.1021/acsnano.1c07621.

28. X. Qin, C. Wu, D. Niu, et al., "Peroxisome Inspired Hybrid Enzyme Nanogels for Chemodynamic and Photodynamic Therapy," *Nature Communications* 12 (2021): 5243, https://doi.org/10.1038/s41467-021-25561-z.

29. E. C. Cheung and K. H. Vousden, "The Role of ROS in Tumour Development and Progression," *Nature Reviews Cancer* 22 (2022): 280–297, https://doi.org/10.1038/s41568-021-00435-0.

30. S. W. Linderman, L. DeRidder, L. Sanjurjo, et al., "Enhancing Immunotherapy With Tumour-Responsive Nanomaterials," *Nature Reviews Clinical Oncology* 22 (2025): 262–282, https://doi.org/10.1038/s41571-025-01000-6.

31. S. Tian, H. Li, Z. Li, et al., "Polydiacetylene-Based Ultrastrong Bioorthogonal Raman Probes for Targeted Live-Cell Raman Imaging," *Nature Communications* 11 (2020): 81, https://doi.org/10.1038/s41467-019-13784-0.

32. S. Gao, Y. Zhang, K. Cui, et al., "Self-Stacked Small Molecules for Ultrasensitive, Substrate-Free Raman Imaging In Vivo," *Nature Biotechnology* 43 (2025): 936–947, https://doi.org/10.1038/s41587-024-02342-9.

33. Q. Zhou, J. Xiang, N. Qiu, et al., "Tumor Abnormality-Oriented Nanomedicine Design," *Chemical Reviews* 123 (2023): 10920–10989, https://doi.org/10.1021/acs.chemrev.3c00062.

34. Z. Ge, Y. Tan, and H. Xu, "Elemental Selenium/Tellurium in Polymer Assemblies: Responsive Innovation," *Polymer Science & Technology* 2 (2026): 79–93, https://doi.org/10.1021/polymscitech.5c00062.

35. G. Zhou and M. Li, "Near-Infrared-II Plasmonic Trienzyme-Integrated Metal–Organic Frameworks With High-Efficiency Enzyme Cascades for Synergistic Trimodal Oncotherapy," *Advanced Materials* 34 (2022): 2200871.

36. W. Huang, L. Zhang, J. Sun, et al., "Hypoxia Reversion by Low-Immunogenic Ultra-Acid-Sensitive Comicelles of Protein–Polymer Conjugates Sensitizes Tumors to Photodynamic Therapy," *Journal of the American Chemical Society* 146 (2024): 7543–7554, https://doi.org/10.1021/jacs.3c13501.

37. R. R. Pandey, Y. Guo, Y. Gao, and C. C. Chusuei, "A Prussian Blue ZnO Carbon Nanotube Composite for Chronoamperometrically Assaying H_2O_2 in BT20 and 4T1 Breast Cancer Cells," *Analytical Chemistry* 91 (2019): 10573–10581, https://doi.org/10.1021/acs.analchem.9b01636.

38. R. F. Bader, "A Quantum Theory of Molecular Structure and Its Applications," *Chemical Reviews* 91 (1991): 893–928, https://doi.org/10.1021/cr00005a013.

39. M. B. Smith, *March's Advanced Organic Chemistry: Reactions, Mechanisms, and Structure*, 7th ed., Wiley, (2013), p. 872.

40. W. Zeng, T. T. Tan, Y. Benseghir, M. R. Reithofer, J. M. Chin, and J. Y. Lim, "Aerobic Photodegradation of Pyrene-Based Metal–Organic Framework NU-1000 to Terephthalic Acid," *Chemistry of Materials* 37 (2025): 3531–3541, https://doi.org/10.1021/acs.chemmater.5c00520.

15213773, 0, Downloaded from https://onlinelibrary.wiley.com/doi/10.1002/anie.9809366 by National University Of Singapore, Wiley Online Library on [12/11/2026]. See the Terms and Conditions (https://onlinelibrary.wiley.com/terms-and-conditions) on Wiley Online Library for rules of use; OA articles are governed by the applicable Creative Commons License

41. S. Enthaler, "The Iron-Catalyzed Oxidation of Alkynes—1,2-Dione Formation Versus Oxidative Cleavage—A Matter of Temperature," *ChemCatchem* 3 (2011): 1929–1934, https://doi.org/10.1002/cctc.201100206.

42. Z. Zhu and J. H. Espenson, "Oxidation of Alkynes by Hydrogen Peroxide Catalyzed by Methylrhenium Trioxide," *Journal of Organic Chemistry* 60 (1995): 7728–7732, https://doi.org/10.1021/jo00129a010.

43. M. I. Bruce, "Organometallic Chemistry of Vinylidene and Related Unsaturated Carbenes," *Chemical Reviews* 91 (1991): 197–257, https://doi.org/10.1021/cr00002a005.

44. C. P. Yap, J. K. Ng, S. Madrahimov, A. A. Bengali, T. S. Chwee, and W. Y. Fan, "Oxidation of Aromatic Alkenes and Alkynes Catalyzed by a Hexa-Acetonitrile Iron(ii) Ionic Complex $[Fe(CH_3CN)_6][BF_4]_2$," *New Journal of Chemistry* 42 (2018): 11131–11136, https://doi.org/10.1039/C8NJ02226G.

45. M. E. Frisch, G. Trucks, H. B. Schlegel, et al., 2016, "Gaussian 16, Revision C.01," Gaussian, Inc. Wallingford, CT.

46. J. Rittle and M. T. Green, "Cytochrome P450 Compound I: Capture, Characterization, and C-H Bond Activation Kinetics," *Science* 330 (2010): 933–937, https://doi.org/10.1126/science.1193478.

47. S. G. Sligar, "Glimpsing the Critical Intermediate in Cytochrome P450 Oxidations," *Science* 330 (2010): 924–925, https://doi.org/10.1126/science.1197881.

48. K. P. Bryliakov and E. P. Talsi, "Active Sites and Mechanisms of Bioinspired Oxidation with H_2O_2, Catalyzed by Non-heme Fe and Related Mn Complexes," *Coordination Chemistry Reviews* 276 (2014): 73–96, https://doi.org/10.1016/j.ccr.2014.06.009.

49. N. Yadav and D. Chandra, "Mitochondrial DNA Mutations and Breast Tumorigenesis," *Biochimica et Biophysica Acta (BBA)—Reviews on Cancer* 1836 (2013): 336.

50. C. Glorieux, S. Liu, D. Trachootham, and P. Huang, "Targeting ROS in Cancer: Rationale and Strategies," *Nature Reviews Drug Discovery* 23 (2024): 583–606, https://doi.org/10.1038/s41573-024-00979-4.

51. K. Fujita and Y. Urano, "Activity-Based Fluorescence Diagnostics for Cancer," *Chemical Reviews* 124 (2024): 4021–4078, https://doi.org/10.1021/acs.chemrev.3c00612.

52. J. C. Hsiao, D. M. Warui, J. J. Kwon, et al., "Deep Mutational Scanning of FDX1 Identifies Key Structural Determinants of Lipoylation and Cuproptosis," *Nature Communications* 17 (2025): 1112, https://doi.org/10.1038/s41467-025-67869-0.

53. T. Xing, L. Li, Y. Chen, et al., "Targeting the TCA Cycle through Cuproptosis Confers Synthetic Lethality on ARID1A-deficient Hepatocellular Carcinoma," *Cell Reports Medicine* 4 (2023): 101264, https://doi.org/10.1016/j.xcrm.2023.101264.

54. A. D. Becke, "Density-functional Thermochemistry. III. The Role of Exact Exchange," *The Journal of Chemical Physics* 98 (1993): 5648–5652, https://doi.org/10.1063/1.464913.

55. F. Weigend and R. Ahlrichs, "Balanced Basis Sets of Split Valence, Triple Zeta Valence and Quadruple Zeta Valence Quality for H to Rn: Design and Assessment of Accuracy," *Physical Chemistry Chemical Physics* 7 (2005): 3297, https://doi.org/10.1039/b508541a.

56. A. V. Marenich, C. J. Cramer, and D. G. Truhlar, "Universal Solvation Model Based on Solute Electron Density and on a Continuum Model of the Solvent Defined by the Bulk Dielectric Constant and Atomic Surface Tensions," *Journal of Physical Chemistry B* 113 (2009): 6378–6396, https://doi.org/10.1021/jp810292n.

57. H. Yamakoshi, K. Dodo, A. Palonpon, et al., "Alkyne-Tag Raman Imaging for Visualization of Mobile Small Molecules in Live Cells," *Journal of the American Chemical Society* 134 (2012): 20681–20689, https://doi.org/10.1021/ja308529n.

58. S. Li, T. Chen, Y. Wang, et al., "Conjugated Polymer with Intrinsic Alkyne Units for Synergistically Enhanced Raman Imaging in Living Cells," *Angewandte Chemie International Edition* 56 (2017): 13455–13458, https://doi.org/10.1002/anie.201707042.

59. F. Hu, C. Zeng, R. Long, et al., "Supermultiplexed Optical Imaging and Barcoding with Engineered Polyynes," *Nature Methods* 15 (2018): 194–200, https://doi.org/10.1038/nmeth.4578.

60. T. Nevitt, H. Öhrvik, and D. J. Thiele, "Charting the Travels of Copper in Eukaryotes from Yeast to Mammals," *Biochimica et Biophysica Acta (BBA)—Molecular Cell Research* 1823 (2012): 1580.

61. C. Lee, W. Yang, and R. G. Parr, "Development of the Colle-Salvetti Correlation-energy Formula into a Functional of the Electron Density," *Physical Review B* 37 (1988): 785–789, https://doi.org/10.1103/PhysRevB.37.785.

62. S. Grimme, J. Antony, S. Ehrlich, and H. Krieg, "A Consistent and Accurate Ab Initio Parametrization of Density Functional Dispersion Correction (DFT-D) for the 94 Elements H-Pu," *The Journal of Chemical Physics* 132 (2010): 154104, https://doi.org/10.1063/1.3382344.

63. S. Grimme, S. Ehrlich, and L. Goerigk, "Effect of the Damping Function in Dispersion Corrected Density Functional Theory," *Journal of Computational Chemistry* 32 (2011): 1456–1465, https://doi.org/10.1002/jcc.21759.

64. E. Cancès, B. Mennucci, and J. Tomasi, "A New Integral Equation Formalism for the Polarizable Continuum Model: Theoretical Background and Applications to Isotropic and Anisotropic Dielectrics," *The Journal of Chemical Physics* 107 (1997): 3032.

Supporting Information

Additional supporting information can be found online in the Supporting Information section.

Details of the experiments are summarized in the Supporting Information. The authors have cited additional references within the Supporting Information [54–64].

Supporting File 1: anie75150-sup-0001-SuppMat.pdf.

15213773, 0, Downloaded from https://onlinelibrary.wiley.com/doi/10.1002/anie.98093366 by National University Of Singapore, Wiley Online Library on [12/11/2026]. See the Terms and Conditions (https://onlinelibrary.wiley.com/terms-and-conditions) on Wiley Online Library for rules of use; OA articles are governed by the applicable Creative Commons License